JOURNAL OF PROPULSION AND POWER
Vol. 17, No. 1, January–February 2001

Regression-Rate and Heat-Transfer Correlations for Hybrid Rocket Combustion

Martin J. Chiaverini,* Kenneth K. Kuo,† Arie Peretz,‡ and George C. Harting§
The Pennsylvania State University, University Park, Pennsylvania 16802

A series of static engine firings, thermal pyrolysis experiments, and gas chromatograph/mass spectrometer tests were conducted to investigate the solid-fuel regression rate and heat-transfer behavior in a lab-scale hybrid rocket motor burning hydroxyl terminated polybutadiene/gaseous oxygen. A real-time, X-ray radiography system was used to determine the local, instantaneous regression rates. A data analysis program was developed to help correlate the experimental data. The semi-empirical regression-rate correlation showed that, in addition to convection, radiation from soot and variable fluid properties across the boundary layer had significant effects on regression-rate behavior. The radiant heat flux from soot was relatively more significant under low mass flux and low oxidizer-to-fuel ratio conditions. Radiation from CO_2, H_2O, and CO was quite small compared to convection and soot radiation. The nondimensional regression-rate correlation agreed with the experimental data to within ± 3%. Stanton- and Nusselt-number correlations were also developed and found to depend on both flow regime and radiant heat flux. The regression-rate correlations predicted independent data from both a lab-scale tube burner and the 11-in. (28 cm) JIRAD motor to very reasonable accuracy.

Nomenclature

A	=	Arrhenius preexponential constant, mm/s
B	=	blowing parameter, $\rho_f r/(Gc_f/2)$ or Eq. (20)
B_{mod}	=	modified blowing parameter, $B\exp(q_r''/q_c'')$
c	=	fuel specific heat, J/kg-K
c_f	=	skin-friction coefficient
c_p	=	gas isobaric specific heat, J/kg-K
$\mathcal{D}$	=	mass diffusivity, m^2/s
Da	=	Damköhler number
D_h	=	hydraulic diameter, cm
E_a	=	activation energy, kcal/mol
F	=	function defined in Eq. (22)
G	=	local, bulk mass flux, kg/m^2-s
h	=	enthalpy, J/kg; port height, mm
L	=	length of fuel slab, 58.4 cm
Nu	=	Nusselt number
Pr	=	Prandtl number
p	=	pressure, atm or MPa
q''	=	heat flux, W/m^2
R	=	function defined in Eq. (34)
Re	=	Reynolds number
R_u	=	universal gas constant, kcal/kg-K
r	=	regression rate, mm/s
St	=	Stanton number
T	=	temperature, K
t	=	time, s
u	=	streamwise velocity component, m/s
w	=	fuel web thickness, mm
x	=	axial location, cm
Y_i	=	species mass fraction
α	=	absorptivity
ΔH_f°	=	heat of formation, J/kg
ΔH_r	=	heat of reaction per unit mass reactants, J/kg
ΔH_v	=	heat of vaporization, J/kg
ε	=	emissivity, or turbulence dissipation rate, m^2/s^3
θ	=	temperature ratio, $T_{\text{fl,avg}}/T_s$
κ	=	absorption coefficient
μ	=	viscosity, Ns/m^2
ρ	=	density, g/cm^3
σ	=	Stefan–Boltzmann constant

Subscripts

avg	=	average
c	=	convective
eff	=	effective
fl	=	flame
g	=	gas phase
o	=	oxidizer, or reference
r	=	radiant
s	=	surface or soot
t	=	turbulent

Received 31 March 1999; revision received 1 February 2000; accepted for publication 17 March 2000.

*Ph.D. Candidate, Department of Mechanical Engineering; currently Project Manager, Orbital Technologies Corporation, Space Center, 1212 Fourier Drive, Madison, WI 53717. Member AIAA.

†Distinguished Professor of Mechanical Engineering, Department of Mechanical Engineering. Fellow AIAA.

‡Visiting Professor, Department of Mechanical Engineering; currently at RAFAEL, P.O. Box 2250, (M1), 31021, Haifa, Israel. Associate Fellow AIAA.

§Ph.D. Candidate, Department of Mechanical Engineering. Student Member AIAA.

Introduction

THE classical hybrid rocket motor provides several important safety and operational advantages over both solid-propellant and liquid-propellant motors because the solid fuel and liquid oxidizer are separated physically and stored in separate phases. In contrast to solid-propellant grains, pure solid fuel grains are insensitive to cracks and imperfections, are inert, and are safe to manufacture, store, transport, and load. Hybrid motors can also be throttled for thrust tailoring, shutdown, restart, and mission abort. Because of their high level of safety, vehicles propelled by hybrid motor systems should be more economical to manufacture and launch than current vehicles.

The solid-fuel regression rate represents the key parameter for hybrid fuel grain internal ballistic studies. A thorough understanding of the physical processes that govern solid-fuel regression under various conditions can assist in developing higher performance motors with more attractive operating characteristics. Probably the most influential theory so far for explaining regression-rate behavior was developed by Marxman and colleagues[1–3] over 30 years ago. They based their approach on turbulent combustion over a flat fuel surface. According to their study, the solid-fuel regression rate is governed primarily by convective heat transfer from the flame to the fuel

surface. The local mass flux G is the primary operating parameter governing regression rate in this theory. Both Marxman and Paul et al.[4] later attempted to modify Marxman and Gilbert's original approach to account for density variations across the boundary layer. Marxman and colleagues[2,3] also made allowances for radiant heat flux caused by gas-phase combustion products, but concluded that only a strong source of thermal radiation would significantly alter the regression-rate behavior.

Several more recent investigations have furthered the study of thermal radiation effects in hybrid combustion. Estey et al.[5] found that including a term to account for thermal radiation improved empirical correlations for metal-loaded fuels, whereas convective heat-transfer theory worked best for pure hydrocarbon fuels. Strand et al.[6] measured the total radiant heat flux to the fuel surface in a slab-geometry, lab-scale motor. In contrast to Estey's findings, they concluded that radiation from soot can significantly influence the regression rate of pure HTPB, especially at lower O/F ratios. They also suggested that future experiments consider the variations in thermal radiation with motor pressure and O/F ratio.

At about the same time Marxman and coworkers[1–3] performed their work, Smoot and Price[7–9] conducted a large number of experiments which indicated that at relatively low pressures and high mass fluxes the solid-fuel regression rates in hybrids employing fluorinated oxidizers displayed a strong pressure dependence, but only a weak dependence on mass flux. After an extensive investigation they concluded that oxidizer transport to the fuel surface and subsequent first-order heterogeneous reactions were responsible for the observed pressure dependence. Their correlation predicted the experimental regression rates to within ±40%. However, both Kosdon and Williams[10] and Muzzy[11] attributed the pressure dependence to finite-rate gas-phase chemical kinetics, while Rastogi and Deepak[12] suggested that heterogeneous reactions at the fuel surface could be responsible for this phenomenon. Citing a mismatch between pyrolysis data obtained in a hybrid motor and from various thermal pyrolysis studies, Kumar and Stickler[13] also considered the possibility of fuel surface attack by unburnt oxidizer passing through the boundary layer. Miller[14] derived an expression, based on both chemical kinetic and gasdynamic variables, that successfully correlated Smoot and Price's data to within the accuracy of their experiments.

Though hybrid rocket motors have been investigated by a number of exceptional researchers over the years, various technical gaps still exist in the literature. Questions still persist as to the extent and nature of radiant heat transfer, gas-phase kinetics, and port geometry effects on regression rate. Scaling effects also remain an area of interest. For example, Estey et al.[5] found that extrapolating simple correlations to different sized motors often resulted in very large errors. Although engineering expressions, such as $r = aG_o^n$, have often been developed to describe the experimental results from particular motors, empirical regression-rate correlations, which reflect the complex nature of hybrid combustion processes, are lacking for modern fuels.

This article discusses recent results obtained from a series of investigations conducted at The Pennsylvania State University on solid-fuel regression-rate behavior in a classical hybrid rocket motor. The main objective of the study was to provide a better understanding of the physical processes that may influence solid-fuel regression-rate behavior under various conditions. During the initial investigation, a lab-scale hybrid motor was designed, constructed, and tested to obtain a large database of local, real-time regression rates and fuel temperatures over a range of operating conditions. Data reduction procedures and preliminary dimensional correlations were developed to describe the solid-fuel regression rates.[15,16] Later, a series of thermal pyrolysis tests was conducted using a rapid-heating technique to obtain pyrolysis laws and to quantify the products of fuel pyrolysis for various solid-fuel formulations.[17] These various experimental results were then combined with a computational scheme to develop dimensionless regression-rate and heat-transfer correlations and to assist in interpreting the data. This paper discusses the results of the combined experimental/computational analysis and presents a set of dimensionless regression-rate and heat-transfer correlations for the hybrid rocket motor. The predicted regression rates from these correlations also compared favorably to data for a lab-scale tube burner[18] and the JIRAD 11-in. hybrid motor.[19]

Method of Approach

Experimental Methods

The windowed, slab-geometry hybrid motor, shown schematically in Fig. 1, has been described in detail in previous papers.[15,16] The motor utilized two opposing fuel slabs each 58.4 cm long and 7.62 cm wide with a uniform initial web thickness of either 4.28 or 4.45 cm, corresponding to port heights of 1.27 or 0.89 cm, respectively. The motor operating conditions were within the range of interest for practical applications: G_o up to 530 kg/m^2-s, p up to 55 atm, L/D_h of about 40, and O/F ratio between 1.5 and 3.5. Both real-time, X-ray radiography and ultrasonic pulse-echo systems (UST) were used to deduce the local, instantaneous solid-fuel regression rates. X-ray radiography was limited to one of the two viewing windows per test. Several embedded 25-μm microthermocouples (TC) were used to measure fuel temperature profiles at various axial locations. Pressure transducers (PT) provided the motor pressure history along the motor port. The tests discussed here focused on HTPB/GOX combustion; however, metallized fuels using both conventional aluminum and explosively formed aluminum powder (Alex) were also tested.[15–17]

The thermal pyrolysis test rig employed a rapid, conductive-heating technique wherein a hot, copper cylinder (1.27 cm in diameter, 7.62 cm in length) was dropped from a tube furnace to the surface of a small solid-fuel strand (typically 0.5 cm in diameter by 1.5 cm in length) to initiate and sustain thermal pyrolysis.[17] The cylinder had a selected initial temperature in the range of 800–1300 K. The fuel strands were situated in a windowed chamber filled with nitrogen to provide a less reactive environment. Most tests were conducted at atmospheric pressure. Regression rates were determined using video images of the pyrolysis process, while micro TCs provided the pyrolyzing surface temperature. Various HTPB-based solid fuels were tested, including pure HTPB. Arrhenius parameters were obtained by correlating the regression rates and surface temperatures. A gas chromatograph/mass spectrometer system with flash-heating pyrolysis oven was employed to identify and quantify the pyrolysis products of the solid fuels. The product concentrations were found to depend strongly on temperature. Reference 17 discusses the results of this study in detail.

Analytical Methods

In addition to the experimental results, several analytic techniques were employed to obtain the variables of interest necessary to provide a thorough analysis of the heat flux and solid-fuel regression-rate behavior in the hybrid motor. The main objective of the analysis was to calculate dimensionless numbers for use in correlating the experimental data. To accomplish this task, it was first necessary to determine the relative importance, under different operating conditions, of the convective and radiative heat fluxes to the solid-fuel surface. Based on initial studies of the experimental hybrid motor data, which indicated a regression-rate pressure dependence in the low mass flux range[16] and on previous studies by Strand et al.,[6] the radiant heat flux to the solid-fuel surface was expected to contribute in a nonnegligible manner to the overall combustion process, even for nonmetallized HTPB.

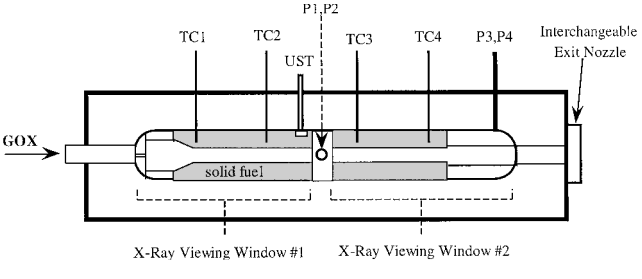

Fig. 1 Windowed, lab-scale hybrid motor.

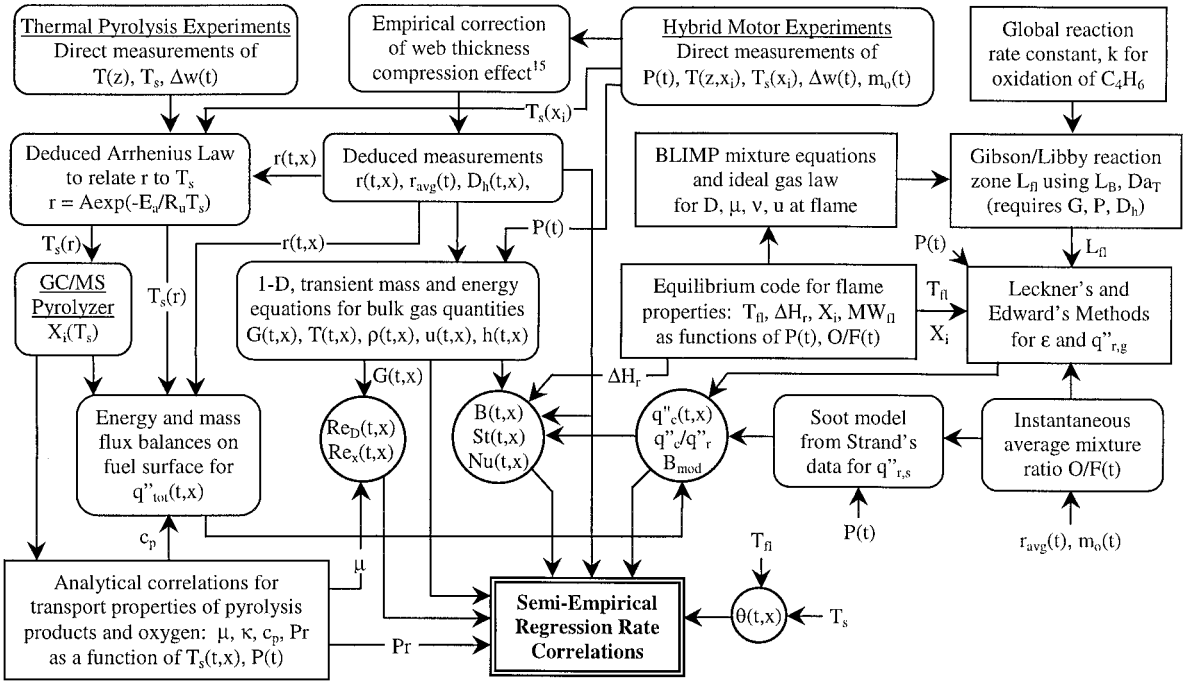

Fig. 2 Schematic flowchart of overall method of approach.

Figure 2 summarizes the relationship among the various analyses and experimentally deduced quantities employed during the present study. The round-cornered boxes indicated experimentally based techniques, the sharp-cornered boxes represent analytical or theoretical analyses, and the circles represent the major results and dimensionless parameters of interest. The diagnostic instruments integrated into the lab-scale hybrid motor directly measured motor pressure history, subsurface fuel temperature profile, surface temperature, local, instantaneous solid-fuel web thickness and port height, and instantaneous oxidizer flow rate into the motor. The local, instantaneous regression rates were deduced using web thickness measurements from the real-time, X-ray radiography video images.[15] The thermocouple array, however, gives only discrete surface temperature measurements at a single time, i.e., the time at which a given thermocouple junction passes through the pyrolyzing fuel surface. A pyrolysis law in Arrhenius form, deduced using data from both the hybrid motor and conductive heating tests, was therefore used with the local, instantaneous regression rates to obtain the corresponding local, instantaneous surface temperatures. The pyrolysis law is given by

$$r = A \exp(-E_a/R_u T_s) \tag{1}$$

where, for pure HTPB, $E_a = 4.91$ kcal/mole and $A = 11.04$ mm/s for T_s greater than 722 K.[17]

Calculation of Total Heat Flux

Energy and mass-flux balances were used to determine the local heat flux to the fuel surface:

$$q''_{\text{tot}} = q''_c + q''_r = \rho_f r \left(\sum_i^n Y_i \Delta H^o_{f,i} - \Delta H^o_{f,\text{HTPB}} \right)$$

$$+ \rho_f r \left(\sum_i^n Y_i \int_{T\text{ref}}^{Ts} c_{p,i}\, \mathrm{d}T \right) \tag{2}$$

where q''_{tot} is caused by both convection and radiation. In deriving Eq. (2), the assumption was made that the species diffusion velocities leaving the fuel surface and the kinetic energy terms associated with fuel regression and vaporization were negligible. The local surface temperature history, deduced using Eq. (1) and the measured fuel regression history, the pyrolyzed species mass fractions (themselves a function of temperature), deduced from the mole fractions measured in the gas chromatograph/mass spectrometer (GC/MS) tests,[17] and thermophysical data for each of the pyrolyzed species were all used to calculate q''_{tot} in a local, instantaneous manner. The heat of formation of HTPB was taken as -2.97 kcal/mol, assuming a molecular weight of 100 g/mol. Polynomial expressions for the individual species' isobaric specific heats $c_{p,i}$ were taken from Ref. 20 and used in the integral term of Eq. (2).

Both the pyrolysis kinetics and the pyrolyzed species concentrations can have nonnegligible effects on the total and convective heat-flux calculations. Using the E_a (4.91 kcal/mol) and A (11.04 mm/s) values just cited, Eq. (1) indicates that a regression rate of 0.5 mm/s, for example, corresponds to a surface temperature of about 798 K, whereas regression rates of 1 and 1.5 mm/s require surface temperatures of 1029 and 1238 K. However, the kinetic parameters listed in Ref. 21, $E_a = 16.9$ kcal/mol and $A = 3250$ mm/s, provide different results. For $r = 0.5$, 1, and 1.5 mm/s the corresponding surface temperatures are 969, 1052, and 1107 K, respectively. These calculations in turn affect the heat-flux calculations. A sensitivity analysis using typical experimental data showed that using the Ref. 21 kinetics altered the total heat-flux calculations by ± 5 to $\pm 10\%$. The effects of pyrolyzed species concentrations were also examined by calculating total heat fluxes assuming that 100% of the pyrolyzed species were 1,3-butadiene gas, rather than the mixure obtained using the GC/MS system.[17] Calculated total heat fluxes increased by about 10% because 1,3-butadiene has, on average, a higher heat of formation (2037 J/g) than the other pyrolysis products identified in Ref. 17. Therefore, the analysis of HTPB hybrid fuel data should include a consideration of all major pyrolysis products, not only 1,3-butadiene.

Calculation of Radiant Heat Flux Caused by Gas-Phase Products

The radiant heat-flux component in Eq. (2) may originate from various sources: the gaseous products of combustion, such as CO_2 and H_2O; soot produced in the motor from the incomplete burning of solid fuel; and metallic particles liberated from the pyrolysis of metallized solid fuel. Because the regression-rate and heat-transfer analysis focused on pure HTPB fuel, the current study did not consider this last radiation source.

The radiant heat transfer to the fuel surface originating from the gaseous combustion products can be calculated by first determining

the gas-phase emissivity. For the case of a solid hydrocarbon fuel/oxygen combustion system, CO_2, H_2O, and CO represent the most important radiating product gases.[22,23] To calculate the appropriate emissivity, the assumption was made that the only significant thermal radiation originated at the reaction zone where the gas composition can be reasonably well characterized using a chemical equilibrium code. (However, thermochemical equilibrium calculations could underestimate the amount of CO_2 and H_2O caused by the formation of soot in the product. The effect of this underestimation is probably not significant for radiant heat-flux calculations because the majority of the thermal radiation originates from soot, as will be shown later.) The flame was therefore treated as a source of thermal radiation, whereas any radiation from other zones of the boundary layer and core flow was ignored. This approach was justified on the basis that the flame represents the hottest region of the flow and also contains the highest concentration of the radiating combustion products. The oxidizer-rich boundary-layer zone above the flame probably emits little radiation because it consists mainly of O_2 and is also somewhat cool compared to the flame, as shown by the numerical results of Venkateswaran and Merkle.[24] The fuel-rich zone between the fuel surface and flame consists of both pyrolyzed hydrocarbon fuel vapors (which can emit and absorb thermal radiation over a wide temperature range) and some combustion products that have diffused from the flame toward the fuel surface. However, radiation from this thin zone to the surface was also ignored because these gases also have relatively low temperature with respect to the flame. In summary then, only the combustion products CO_2, H_2O, and CO at the flame were assumed to emit significant radiation to the fuel surface, and this simplification leads to the following analysis.

Leckner's empirical correlations[23] were used to estimate the emissivity of both CO_2 and H_2O, whereas Edwards exponential wide-band radiation model[23] was used to determine the emissivity of CO. For Leckner's method the emissivity at atmospheric pressure is first calculated:

$$\varepsilon_o(p_a,\, p = 1\cdot\text{bar},\, T_g) = \exp\left\{ \sum_{i=0}^{m}\sum_{j=0}^{n} c_{ji}\left(\frac{T_g}{T_o}\right)^j \times\left[\log_{10}\frac{p_a L_g}{(p_a L_g)_o}\right]^i\right\} \tag{3}$$

where the reference temperature T_o equals 1000 K and $(p_a L_g)_o$ equals 1 bar-cm. The term $p_a L_g$ is called the partial pressure path length of the gas component and represents the product of partial pressure and a geometric path length, such as the thickness of the gas layer. The emissivity at the actual pressure is calculated from

$$\frac{\varepsilon(p_a L_g,\, p,\, T_g)}{\varepsilon_o(p_a L_g,\, 1\cdot\text{bar},\, T_g)} = 1 - \frac{(a-1)(1-P_E)}{a+b-1+P_E} \times \exp\left\{-c\left[\log_{10}\frac{(p_a L_g)_m}{p_a L_g}\right]^2\right\} \tag{4}$$

where the pressure term P_E depends on the total pressure, partial pressure of the gas component under consideration p_a, and the temperature ratio T_g/T_o. The partial pressures are readily found from the measured pressure and equilibrium mole fractions. The correlation parameters in Eqs. (3) and (4) for H_2O and CO_2, as well as Edward's method for CO, are given in detail by Modest.[23]

As shown in Fig. 2, the radiation models require the total gas pressure, species partial pressures or mole fractions, gas temperature, and path length L_g as inputs. A chemical equilibrium code was used to determine the theoretical flame temperature and species mole fractions as a function of instantaneous pressure and O/F ratio. The instantaneous O/F ratio was calculated using the instantaneous GOX flow rate into the motor and the instantaneous fuel mass-flow rate, based upon the known, spatially integrated regression rate. The assumption was made that the motor had a uniform O/F ratio at each instant of time because the local O/F ratio at the flame is not particularly well known. The experimentally measured motor pressure was combined with the equilibrium mole fractions to yield the CO_2, H_2O, and CO partial pressures.

Because only the combustion products at the diffusion flame zone were considered to generate significant radiation, the reaction zone thickness L_{fl} represents the appropriate path length for use in the gas-phase radiation calculations. For turbulent diffusion flames Gibson and Libby[25] used an analytic expression to calculate the thickness of the flame zone as a function of the Damköhler number Da_T and the Batchelor length scale of turbulence L_B:

$$L_{\text{fl}} \sim L_B (Da_T)^{\frac{1}{4}} \tag{5}$$

where

$$L_B = (\nu D^2/\varepsilon)^{0.25} \tag{6}$$

and

$$Da_T = (\nu k^2/\varepsilon)^{0.5} \tag{7}$$

where ε should not be confused with the emissivity. In Eqs. (6) and (7) the molecular diffusivity and kinematic viscosity of the gas mixture at the flame were calculated using the boundary-layer integral matrix procedure (BLIMP) mixture equations described by Kuo.[26] For the global reaction of 1,3 butadiene gas (the most abundant pyrolysis product of HTPB) and gaseous oxygen, Cheng et al.[27] gives the rate constant, in s^{-1}, as

$$k = 8.80\times 10^{11}\exp(-15{,}200/T) \tag{8}$$

with T in K, which was used in calculating Da_T. Turns[28] suggests estimating ε with

$$\varepsilon \sim 3u_{\text{rms}}'^3 \big/ 2l_o \tag{9}$$

The integral turbulence length scale l_o can be estimated at about an order of magnitude smaller than the characteristic length scale of the problem, which, for the present purposes, is the local, instantaneous port height (distance between the fuel slabs). Therefore, it was assumed that $l_o \sim 0.1h$. The local value of h was measured using the real-time X-ray radiography system. Similarly, u'_{rms} is about an order of magnitude smaller than the mean streamwise velocity component, such that $u'_{\text{rms}} \sim 0.1u$, where the velocity of interest is the gas velocity in the flame zone u_{fl}. Strand et al.[29] have confirmed this estimate with hot-wire anemometry measurements during nitrogen cold-flow tests in a lab-scale hybrid motor. The gas velocity in the flame zone can be approximated by

$$u_{\text{fl}} \sim G/[(pM_{\text{fl}})/(R_u T_{\text{fl}})] \tag{10}$$

where the local bulk mass flux is deduced using a one-dimensional, transient analysis,[30] and T_{fl} and MW_{fl} are determined from chemical equilibrium calculations. G represents the local, bulk (average) streamwise mass flux across the port.

Despite the rough estimates used in calculating the flame thickness, Eq. (5) gives quite reasonable results with respect to experimental measurements. Schlieren measurements in Ref. 3 have shown that the reaction zone in an atmospheric hybrid motor is approximately 0.8–1.6 mm thick. Similarly, typical flame thickness calculated using the present method was 1–2 mm. In any case, it turned out that the flame emissivity was relatively insensitive to the particular choice of reaction zone thickness.

Because the flame zone has a finite thickness, it seemed reasonable to use a bulk flame temperature in the radiation calculations rather than the theoretical flame temperature, which may represent an overestimation of the average temperature in the flame zone. Temperature profiles from the computational hybrid model developed by Venkateswaran and Merkle in a parallel study[24] were used to show that the bulk temperature across the reaction zone varied from approximately 97 to 91% of the equilibrium flame temperature.

With the motor pressure, species partial pressures, bulk flame temperature, and flame thickness determined from the preceding analysis, the total emissivity of the gas mixture was calculated from

$$\varepsilon_g = \varepsilon_{H_2O} + \varepsilon_{CO_2} + \varepsilon_{CO} - \Delta\varepsilon \tag{11}$$

where $\Delta\varepsilon$ represents a correction factor to account for the fact that CO_2 and H_2O emit radiation in partially overlapping bands.[23] The net thermal radiation transferred to the fuel surface by the combustion products was calculated using

$$q''_{r,g} = \sigma \varepsilon_s \left(\varepsilon_g T_{\text{fl}}^4 - T_s^4\right) \tag{12}$$

where ε_s was 0.95 (Modest's value for glossy rubber[23]). Because typical fuel surface temperatures were on the order of 1000 K and flame temperatures on the order of 3500 K, only a small fraction of the radiant energy was absorbed by the flame.

Calculation of Radiant Heat Flux Caused by Soot

Radiation from particles in hybrid motors has largely been neglected in the past, especially for nonmetallized fuels. However, soot particles can act as effective blackbody radiators, and because soot is commonly associated with hydrocarbon flames, it seems reasonable that some portion of the radiant heat flux may originate from soot. Strand et al.[6] have made similar observations using their lab-scale hybrid motor, which also burned GOX and HTPB. Their experimental data were used to develop an appropriate soot radiation model for the present study. Strand et al.[6] used a calorimeter, radiometer, and infrared thermometer to measure the total heat flux to the fuel surface, radiant heat flux to the fuel surface, and flame temperature, respectively. The operating pressure, average regression rate, and average O/F ratio (between 2 and 3) were also measured. The measured radiant heat flux incident to the fuel surface was thought to originate from both combustion product gases and soot particles.[6] To distinguish the relative magnitudes of radiation from these two sources for use in the present study, Leckner's method and Edward's model, along with the supporting analysis just discussed, were employed to determine the amount of radiation caused by the H_2O, CO_2, and CO product gases in Strand et al.'s[6] measurements. The radiation caused by soot was obtained by subtracting the calculated amount of radiation from the gas-phase combustion products from the total radiation measurements. The results of this analysis indicated that radiation from the gaseous products actually contributed a relatively small amount to the total radiative heat flux. Soot was found to account for approximately 80% of the total radiant heat flux measured by Strand et al.[6]

The soot absorption coefficients were found by assuming that $q''_{r,s}$ could be calculated from

$$q''_{r,s} = \sigma T_g^4 (1 - e^{-\kappa_s}) \tag{13}$$

and that the soot particles were in thermal equilibrium with the surrounding gas. The term in parentheses corresponds to the soot emissivity. The reference gas temperature T_g was taken to be 95% of the equilibrium flame temperature because Strand et al.[6] showed that their measured flame temperature was slightly lower than the calculated adiabatic flame temperature of 3400 K. Use of a reference gas temperature does not imply that all of the soot particles are at this temperature. In general, the soot in the motor should have a temperature distribution. Nevertheless, the reference gas temperature T_g was used to relate the absorption coefficient to the motor operating conditions.

The absorption coefficients calculated using Eq. (13) were correlated with the corresponding pressures and O/F ratios. According to the data of Strand et al.,[6] κ_s exhibited no obvious pressure-dependence, but depended strongly on the measured O/F ratio such that

$$\kappa_s = 0.51 - 0.113\,\text{O/F} \tag{14}$$

Though Strand et al.[6] measured average O/F ratios between 2 and 3, Eq. (14) was assumed valid for the present study where instantaneous O/F ratios ranged from about 1.5 to 3.5. Equation (14) indicates that higher O/F ratios lead to lower soot emissivities because more oxidizer is available to react with the pyrolysis products. Equations (13) and (14) were subsequently used with the instantaneous O/F ratio and bulk flame temperature to determine the radiant heat flux caused by soot particles for the tests under this investigation. Equation (14) applies only for the combustion of oxygen and HTPB. Other fuel and oxidizer combinations may display different sooting trends.

Calculation of Convective Heat Flux

The amount of heat flux caused by convection was determined by subtracting the radiant heat fluxes from the total heat flux:

$$q''_c = q''_{\text{tot}} - q''_{r,g} - q''_{r,s} \tag{15}$$

The relative magnitudes of the heat fluxes under different operating conditions are discussed later.

Several other quantities are required to complete the analysis described in Fig. 2. The local, bulk, instantaneous mass flux was determined using a transient, one-dimensional code that employed the continuity, energy, and ideal gas law equations to finite volumes along the combustion port. The bulk density, temperature, velocity, and enthalpy were also obtained using this method. The molecular transport properties, such as μ, k, $\mathcal{D}$, and c_p, were determined using analytic methods from the BLIMP model.[26]

Discussion of Results

Table 1 shows a summary of the operating conditions and global regression rates for the test firings conducted with the lab-scale hybrid rocket motor. The run times for all tests were between 5 and 10 s. Tests 10 and 16 are not listed in Table 1 because these

Table 1 Summary of lab-scale hybrid motor test firings (averaged data)

Test number	Fuel (top/bottom)	G, kg/m^2-s	P_c, atm	D_h, cm	O/F	r, mm/s	Remarks
1–4	HTPB	——	——	——	——	——	Ignition and checkout
5	HTPB	151.0	40.2	2.64	1.29	1.36	Large p oscillations
6	HTPB	113.5	25.9	3.20	1.88	0.87	Ultrasound
7	HTPB	83.5	26.6	3.24	1.72	0.73	X-ray, ultrasound
8	HTPB	82.2	25.5	3.21	1.67	0.72	X-ray, ultrasound
9	HTPB and HTPB w 0.25% cb[a]	174.4	25.5	3.00	2.06	1.10 and 1.13	X-ray, ultrasound carbon black (cb)
11	HTPB w 0.25% cb[a] and HTPB	117.9	30.4	3.39	2.04	0.92 and 0.92	X-ray, ultrasound carbon black (cb)
12–14	HTPB with Alex	——	——	——	——	——	Effects of Alex
15	HTPB	207.1	32.0	2.86	1.95	1.26	X-ray, ultrasound
17	HTPB	215.9	30.3	2.83	1.93	1.27	X-ray, ultrasound
18	HTPB	171.8	29.6	3.33	2.26	1.24	X-ray, ultrasound
19	HTPB	197.2	31.2	2.97	1.95	1.26	X-ray, ultrasound
20	HTPB	273.5	18.7	2.73	2.05	1.54	X-ray, ultrasound
21	HTPB w 20% Al HTPB	174.1	27.3	3.24	1.96	1.25 1.09	X-ray, ultrasound Effects of 20% Al

[a]Carbon black powder, 75 nm.

firings did not yield reportable data. The effect of carbon black as an opacifying agent (Tests 9 and 11) and the effects of Alex (ultra-fine aluminum) and conventional aluminum as regression-rate enhancing agents (Tests 12–14, 21) were also investigated.[15–17] A more detailed analysis of the regression-rate behavior of the metallized fuels will be reported in a future work.

The global regression rates shown in Table 1 represent a time- and space-average value determined by averaging local pre- and postfiring fuel web thickness measurements. Measurements were made using a caliper at intervals of 1.25 or 2.5 cm along the length of the fuel slabs. These local changes in web thicknesses were also used to calculate the average hydraulic diameters, which included the side walls, as well as the corresponding cross-sectional areas. The mass-flux values listed were similarly calculated by averaging the local mass fluxes. The O/F ratio listed in Table 1 represents the time-averaged mixture ratio that occurs at the end of the fuel slab. The chamber pressure is also a time-average value. Large pressure oscillations on the order of ±25% of the mean pressure were observed for Tests 1–5. A modification to the feed system eliminated the combustion instability, and the remaining tests displayed pressure traces with about ±1% oscillations.

A simple regression-rate correlation was developed using the global (time- and space-averaged) r and G values shown in Table 1. A least-squares analysis of the data yielded

$$r = 0.049G^{0.61} (R^2 = 0.989) \tag{16}$$

The high R^2 value of 0.989 indicates that Eq. (16) accurately represents the experimental data. Equation (16) was developed for nonmetallized HTPB only using the Table 1 data from Tests 6–9, 11, 15, and 17–20. Test 5 was not included because of the large pressure oscillations, which are known to enhance fuel regression rates.[19] Indeed, Eq. (16) predicts a regression rate of 1.05 mm/s for Test 5, whereas the experimental regression rate is 29.5% higher at 1.36 mm/s.

Component Heat-Flux Behavior

The local, real-time regression rates used to calculate heat-flux behavior were found using the X-ray radiography system. Figure 3 shows a typical local regressed fuel web thickness trace and corresponding regression-rate trace. Local fuel web thickness measurements were made from captured video images at frequencies of about 6–7 Hz. Sample X-ray images can be found in Ref. 15. In Fig. 3 the regressed fuel web thickness was fit with

$$w = at^b \tag{17}$$

where t is measured from ignition and a and b are empirical constants. The time of ignition was determined from the pressure trace. The corresponding instantaneous regression rate was found simply by differentiating Eq. (17) with respect to time t to obtain

$$r = \frac{\mathrm{d}w}{\mathrm{d}t} = abt^{b-1} \tag{18}$$

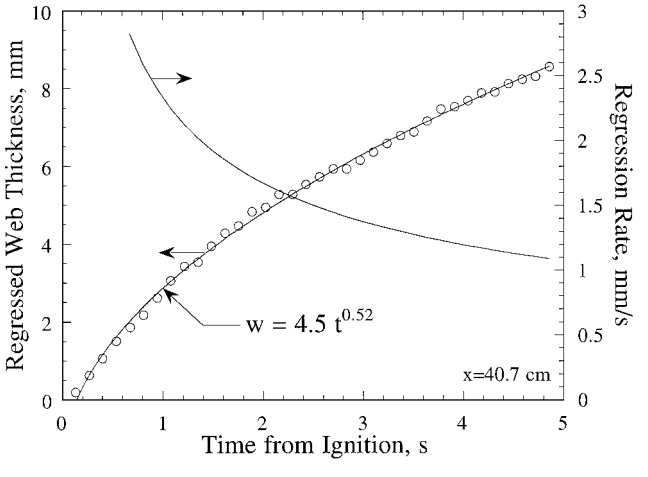

Fig. 3 Typical instantaneous fuel web thickness change and calculated regression rate.

Normally, 12–15 local regression-rate traces, taken at approximately 1.25-cm intervals along a selected region of the fuel slab, were deduced for each test. Reference 15 provides a detailed discussion of the procedures used to deduce the instantaneous regression rates from both the X-ray radiography and ultrasonic pulse-echo systems, including the treatment of the ignition, engine pressurization, and shutdown transients.

Figure 4 shows the Arrhenius plot obtained using surface temperature and corresponding time-averaged regression-rate measurements from both the hybrid motor and the rapid-heating pyrolysis test rig.[17] Reference 17 provides a detailed discussion of the analysis used to obtain Fig. 4. Here, it suffices to note that both sets of data agree well, indicating no mismatch between regression-rate data in the high-pressure, oxidative environment of the hybrid motor and the atmospheric-pressure, nitrogen environment of the thermal pyrolysis test rig. This result suggests that heterogeneous reactions did not play an important role in the overall fuel regression process in the hybrid motor.

The Arrhenius law shown in Fig. 4 was combined with the instantaneous regression-rate database to calculate the total surface heat fluxes. In a parallel effort Venkateswaran and Merkle[24] developed a two-dimensional computational fluid dynamics (CFD) code to numerically simulate the regression and combustion processes in the present hybrid motor and obtained a number of important results. Figure 5 compares the total heat-flux profiles obtained using the current method for Tests 17 and 19 (conducted under similar conditions, but different X-ray viewing regions) with the numerically calculated profile. Except near the inlet to the combustion port, very

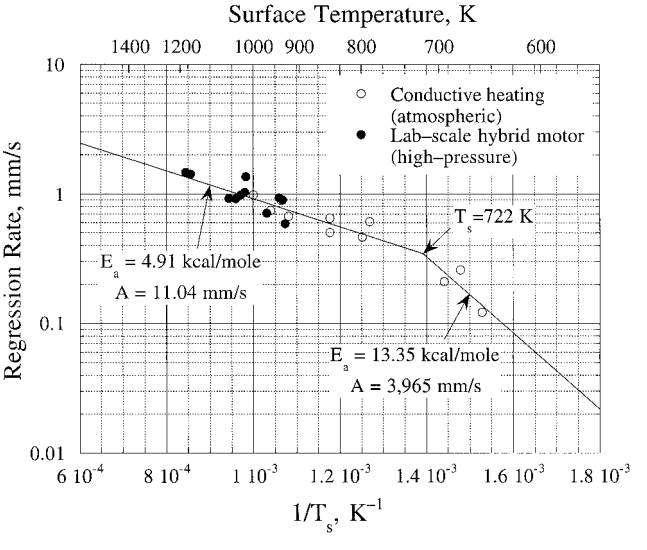

Fig. 4 Arrhenius law for pure HTPB.

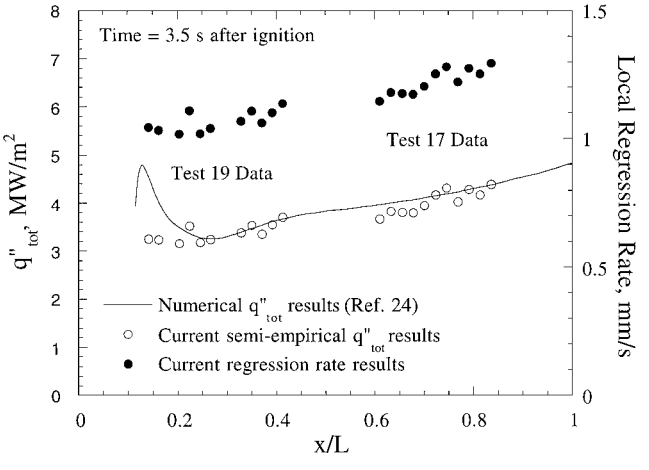

Fig. 5 Comparison of q''_{tot} profiles.

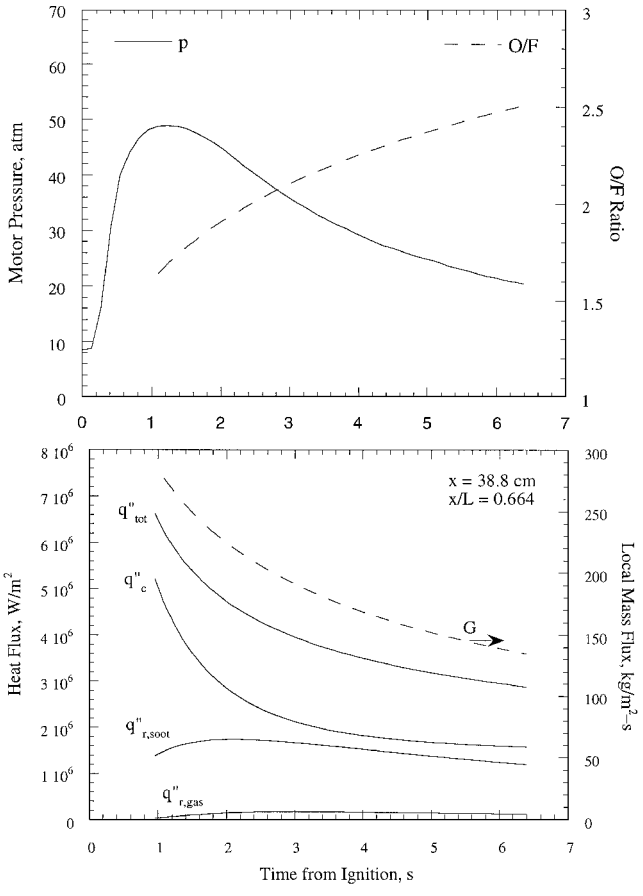

Fig. 6 Component heat-flux behavior with respect to *G*, *p*, and O/F ratio.

reasonable agreement was obtained for both cases. The heat flux tends to increase in the downstream direction because of the continual addition of pyrolyzed fuel and thermal energy generation from combustion. Figure 4 also provides the corresponding regression-rate profiles, which tend to follow the total heat-flux profiles.

The component heat fluxes were determined according to the procedure describe earlier. Figure 6 shows typical results from Test 15, along with the local mass flux, pressure and O/F ratio traces. At higher mass fluxes the convective portion of the total heat flux is relatively large compared to the radiant heat fluxes caused by soot and the gas-phase combustion products. At lower mass fluxes the radiant heat fluxes become relatively more important. Near the beginning of the test, q_c'' accounts for about 80% of q_{tot}'', whereas near the end it is about 60% of q_{tot}''. As the O/F ratio increases during the test, the emissivity caused by soot decreases because a larger amount of oxygen is available to react with the pyrolyzed fuel. However, the O/F ratio also affects the average temperature across the reaction zone, which is the reference temperature for the soot radiation calculations. Thus, the soot radiation initially increases, even though k_s decreases because the flame temperature increases with O/F ratio up to an O/F ratio of about 2.7. The test conditions of Fig. 6 corresponds to a fuel-rich situation. After peaking, the soot radiation then decreases as a result of the inverse relationship between soot emissivity and O/F ratio. On the other hand, equilibrium calculations show that, at fixed pressure and increasing O/F ratio, the reaction of HTPB and O_2 produces higher mole fractions of CO_2 and H_2O at the expense of CO. Because most of the gas-phase radiation originates from CO_2, the overall radiation from gaseous combustion products tends to increase at higher O/F ratio levels. However, the radiation from the gaseous combustion products represents a small portion of the total heat flux over the entire operating range because of the relatively small magnitude of the individual emissivities, shown in Fig. 7. Carbon dioxide contributes most of the gas-phase radiation at all O/F ratios greater than 1.5. In comparison the effective soot emissivity is about 0.2 at an O/F ratio of 2.5.

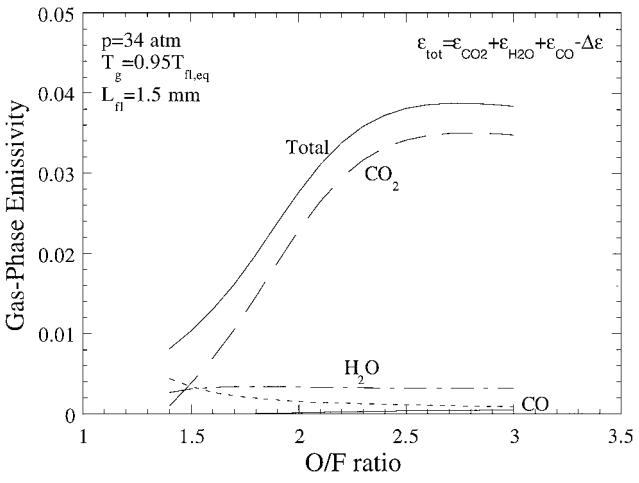

Fig. 7 Components of gas-phase emissivity from flame for typical conditions.

Regression-Rate Correlations

Based on the results of the pyrolysis experiments and heat-flux calculations, it was assumed that the solid-fuel regression rates were governed primarily by heat transfer to the fuel surface via convection and radiation. The possible effects of heterogeneous reactions and rate-limiting gas-phase chemical kinetics were ignored based on the good agreement between the pyrolysis laws obtained from the hybrid motor tests and thermal pyrolysis experiments. Lengelle et al.[31] has also suggested that HTPB regression during practical motor operation (with oxygen) is probably not influenced by gas-phase reaction kinetics.

Drawing on the work of Lees,[32] Marxman and Gilbert[1] used a simple energy flux balance on the fuel surface to show, for a purely convective heat-transfer-governed fuel regression process, that

$$\rho_f r = \frac{q_c''}{(\Delta H_v)_{\text{eff}}} = G \cdot St \cdot B \tag{19}$$

For the present purposes the Stanton and blowing numbers can be defined as

$$St \equiv \frac{q_c''}{G[\Delta H_r + (h_{\text{bulk}} - h_{\text{wall}})]} \tag{20}$$

$$B \equiv \frac{\Delta H_r + (h_{\text{bulk}} - h_{\text{wall}})}{(\Delta H_v)_{\text{eff}}} \tag{21}$$

Marxman assumed that the boundary-layer reaction zone did not affect the velocity profile and defined *St* in terms of *G* at the flame, leading to an alternate definition of *B*.[1–3] The blowing parameter can be interpreted as the ratio of the thermal energy of the main stream relative to the surface to the thermal energy required to pyrolyze a unit mass of solid fuel. Equation (21) is similar to definitions given by a number of other researchers.[9,33]

Equation (19) states that the convective heat flux provides the energy required to pyrolyze a unit mass of solid fuel at a given regression rate. However, the current heat-transfer analysis revealed that thermal radiation plays a nonnegligible role in the overall regression process. To account for this additional driving force for solid-fuel regression, Marxman and coworkers[2,3] suggested that a correction factor be included on the right side of Eq. (19), such that

$$\rho_f r = \frac{q_c''}{(\Delta H_v)_{\text{eff}}}\left[\frac{q_r''}{q_c''} + \exp\left(-\frac{q_r''}{q_c''}\right)\right] \tag{22}$$

As noted by Marxman, it is important to understand that the convective and radiant heat fluxes reaching the fuel surface are not independent of one another. Radiant heat flux causes additional wall blowing, which acts to block the convective heat flux, causing the regression rate to decrease. When the regression rate decreases, the blocking effect decreases, and convective heat flux to the fuel surface increases, and so on. In the absence of radiation, the entire

term in square brackets in Eq. (22) becomes unity, as expected for a purely convective heat-transfer situation.

Equation (19) was also modified to account for the effects of variable fluid and transport properties in the boundary layer, which may have some effect on solid-fuel regression.[3,4] Following the method suggested by Kays and Crawford,[34] a temperature factor θ, representing the ratio of average flame to surface temperature, was employed to account for these effects. These temperatures seem appropriate because the reaction zone represents the effective boundary for heat transfer to the fuel surface. Using property ratios to account for variable fluid and transport property effects is a relatively standard technique for flows involving combustion or high Mach numbers. The final equation chosen to correlate the experimentally determined regression rates had the form:

$$\rho_f r/G = aStB\theta^b\left\{c(q_r''/q_c'')^d + \exp\left[-c(q_r''/q_c'')^d\right]\right\}$$
$$= aStB\theta^b[F(q_r''/q_c'')] \tag{23}$$

where a, b, c, and d represent empirical parameters. Although Marxman suggested that c and d were both unity for hybrid systems with $B > 5$, these two parameters were allowed to vary to fit the data because the local, instantaneous values of B were sometimes less than five for some of the tests conducted during the current investigation.

A least-squares fit of the experimental data fit Eq. (23) yielded $a = 0.524$, $b = 0.6$, $c = 1.3$, and $d = 0.75$. Figure 8 shows that Eq. (23) predicts the experimental results to within $\pm 3\%$, which is about the same as the estimated measurement error. Though Eq. (23) does not have a particularly simple form, each of the factors has a definite physical significance: St and B account for convective heat flux to the fuel surface in the presence of wall blowing, the term in brackets accounts for the additional driving force of thermal radiation and θ accounts for effects of fluid and transport property variations in the shear layer below the reaction zone.

Figure 9 shows typical flame and surface temperature results to illustrate the qualitative behavior of the temperature correction factor. The temperature ratio increases during the test, mainly because of the decrease in surface temperature. The surface temperature drops because of a decrease in convective heat flux (see Fig. 6) accompanying the decrease in local mass flux. The bulk flame temperature varies somewhat as a result of changes in instantaneous O/F ratio and pressure. For the typical temperatures shown in Fig. 9, $\theta^{0.6}$ ranged from 1.7 to 2.0.

Figure 10 shows the behavior of the radiative term and the corresponding term suggested by Marxman and coworkers.[2,3] Up to a q_r''/q_c'' value of 2.86, the function $F(q_r''/q_c'')$ shown in Eq. (23) is larger than Marxman's term. When $q_r''/q_c'' = 1.0$, $F(q_r''/q_c'')$ is about 15% larger than Marxman's. Above 2.86, Marxman's term becomes larger. For the tests conducted here the calculated values of q_r''/q_c'' were most typically between 0.5 and 1.0. Therefore, radiant heat flux was generally found to be of the same order as convective heat flux.

As discussed in the Introduction, many investigations have used simple correlations, such as the well-known $r = aG^n$, to describe a particular set of experimental data. Though such regression-rate correlations may describe the time-averaged data to acceptable accuracy, large errors often result when applied to other test data.[5] Figure 11 shows the results of Eq. (16), developed using the average data shown in Table 1, applied to both the instantaneous and average regression-rate data of the current investigation. The correlation

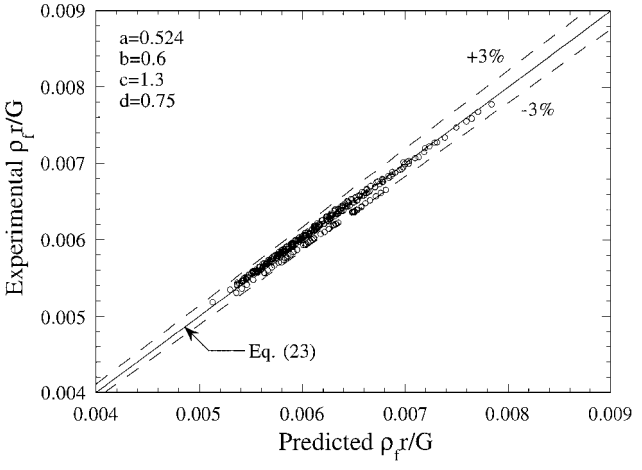

Fig. 8 Regression-rate correlation using Eq. (23).

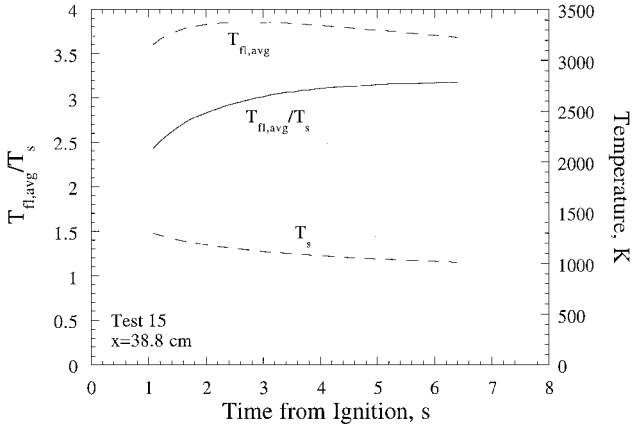

Fig. 9 Typical temperature ratio behavior.

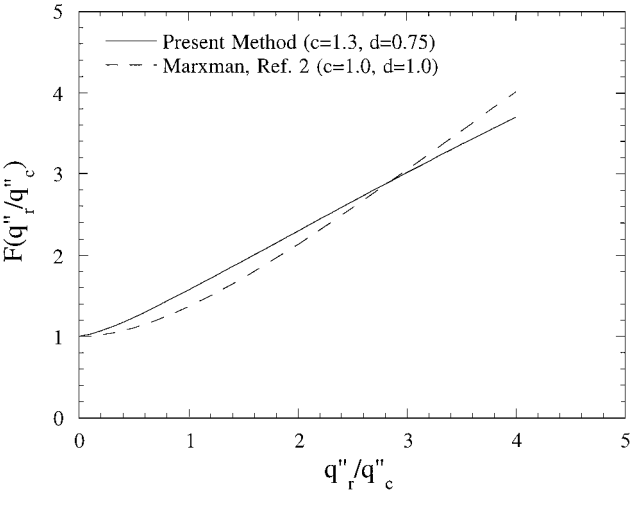

Fig. 10 Comparison of radiation terms.

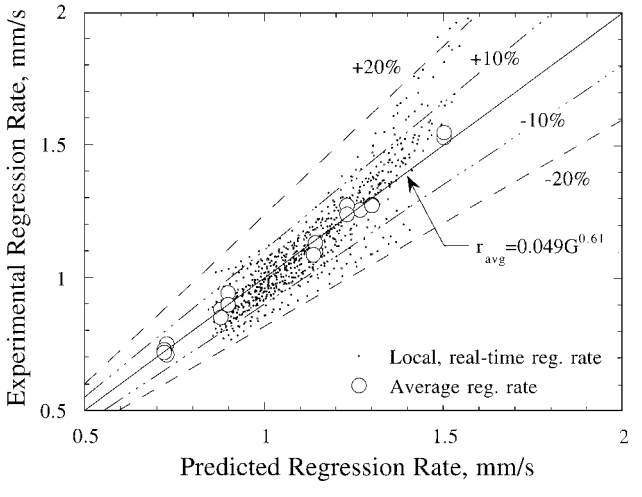

Fig. 11 Illustration of inadequacy of using power law expression generated from average regression rates to correlate instantaneous regression rates.

fairly accurately describes the average regression-rate data. However, the local, real-time data do not fit nearly as well and frequently display errors up to ±20%. Comparing Figs. 8 and 11, it is clear that Eq. (23) not only provides physical insight into the regression-rate behavior, but also describes the experimental data to much better accuracy. The expression $r = aG^n$ does not properly represent the physical nature of the solid-fuel regression rates.

Heat-Transfer Correlations

To illustrate the effects of wall blowing on convective heat transfer to the fuel surface, the Stanton number in Eq. (23) can be multiplied and divided by the reference Stanton number for turbulent pipe flow,[22] where

$$St_o = 0.023 Re_D^{-0.2} Pr^{-0.7} \tag{24}$$

Using Eq. (24) in Eq. (23) and rearranging yields

$$\rho_f r/G = 0.0155 Re_D^{-0.2} (St/St_o) B\theta^{0.6} \left\{1.3(q_r''/q_c'')^{0.75} + \exp\left[-1.3(q_r''/q_c'')^{0.75}\right]\right\} \tag{25}$$

where the bulk gas Prandtl number was absorbed into the leading constant because it did not vary significantly from 0.7.

The Stanton-number ratio gives an indication of the amount of convective heat flux reaching the surface under the hybrid motor conditions with respect to that expected for simple turbulent pipe flow without the additional effects of wall blowing and boundary-layer combustion. The Stanton-number ratio can itself be correlated with other parameters, such as the blowing parameter. Based on the results of several researchers, Marxman and coworkers[2,3] concluded that for $5 < B < 100$

$$St/St_o = 1.2B^{-0.77} \tag{26}$$

The inverse relationship shown in Eq. (26) implies that higher blowing numbers cause greater blockage of convective heat transfer to the fuel surface. Given the relative importance of the radiant heat flux revealed by the current analysis, it seems logical that radiant heat transfer can also affect St/St_o. For situations involving significant radiation, Marxman showed that

$$B_{\text{rad}} = B \cdot \exp[1.3(q_r''/q_c'')] \tag{27}$$

again for $5 < B < 100$ (Ref. 2). A new blowing number was therefore defined for the present analysis as

$$B_{\text{mod}} = B \cdot \exp[n(q_r''/q_c'')] \tag{28}$$

where n represents an empirical constant. For the present analysis it was found that $n = 1.0$ gave the best correlation results.

Figure 12 shows a plot of St/St_o vs B_{mod} with $n = 1.0$. Several characteristics of the Stanton-number ratio behavior are immediately apparent. First, the data set available from the downstream

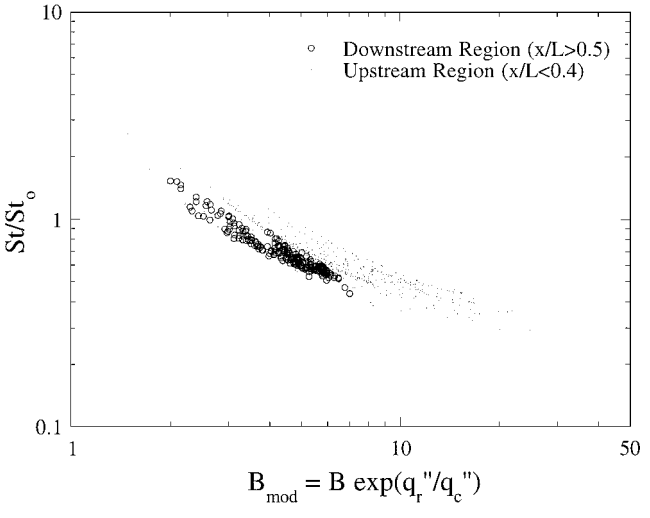

Fig. 12 St/St_o behavior with respect to B_{mod}.

X-ray viewing window tend to display lower values than the upstream data at the same value of B_{mod}. Second, the St/St_o ratio often exceeds unity, even in the presence of wall blowing. Both of these observations can be explained by a closer inspection of the boundary-layer combustion process.

A reasonable explanation for the first characteristic concerns the development of the boundary-layer flow between the two opposing fuel slabs. If the downstream region was fully developed while the upstream region was subject to developing boundary layers, the convective heat-transfer behavior in each of the two regimes could prove different, implying the need for two separate correlations. For each test, calculations were made of the local, instantaneous boundary-layer thickness using two different equations:

$$\delta = 0.37 \times Re_x^{-0.2} \tag{29}$$

and

$$\delta = x\{[0.0281(1 + B)/I][\ln(1 + B)/B]\}^{0.8} Re_x^{-0.2} \tag{30}$$

where

$$I = \frac{7(1 + 1.3B + 0.364B^2)}{72(1 + 0.5B)^2} \tag{31}$$

Equation (29) represents the standard expression for the thickness of a boundary layer over a turbulent flat plate in the absence of combustion and wall blowing and serves as a limiting case. Marxman presented Eqs. (30) and (31) to account for the effects of blowing and combustion on the boundary-layer thickness.[3] Wall blowing should tend to increase the boundary-layer thickness over that of the reference case. The modified blowing parameter B_{mod} was used here in place of B in Eq. (30) and (31) to account for the effects of radiation.

To estimate where the boundary layers merged, the calculated local boundary-layer thickness was compared to the experimentally measured port height (distance between the two fuel slabs). For the regression-rate data obtained in the downstream region of the motor, beyond about $x/L = 0.5$ both Eqs. (29) and (30) predicted that the boundary layers were merged at the beginning of the test when the port height is small. Toward the end of the tests, when port height has grown as a result of fuel regression, Eq. (29) sometimes predicted nonmerged boundary layers, but Eq. (30) always indicated fully developed flow. However, for $0 < x/L < 0.4$ the calculated local boundary-layer thickness was always less than half of the local port height. Thus, it seems that the boundary layers merged for each test somewhere along a region of the combustion port between $0.4 < x/L < 0.5$. This region was blocked from X-ray viewing by a motor structural support element between the two windows. This location corresponds to a instantaneous x/h range of about 12–24, depending on test conditions. Based on these results, it was concluded that developing flow probably prevailed in the upstream portion of the motor, from the fuel slab leading edge down to at least $x/L = 0.4$, while the flow in the downstream portion was fully developed. Because convective heat-transfer rates in the developing region of an internal flow are higher than those in the fully developed region,[34] it seems logical that the upstream St/St_o values tend to be somewhat higher than those in the downstream region at the same value of B_{mod}.

Note also from Fig. 12 that the Stanton number is sometimes larger than the reference Stanton number, i.e., $St/St_o > 1$. This finding suggests that the actual shear flow is quite different from simple turbulent pipe flow. The effects of axial acceleration as a result of boundary-layer growth in a confined space, the addition of heat and mass in the downstream direction, and variable fluid properties across the boundary layer can all affect the boundary-layer behavior. Previous researchers have found smaller Stanton-number ratios at similar blowing parameters (not including radiation), but their experiments did not take into account the hybrid boundary-layer effects encountered in realistic motors and considered mainly flat plate-type flows over single fuel slabs.[3]

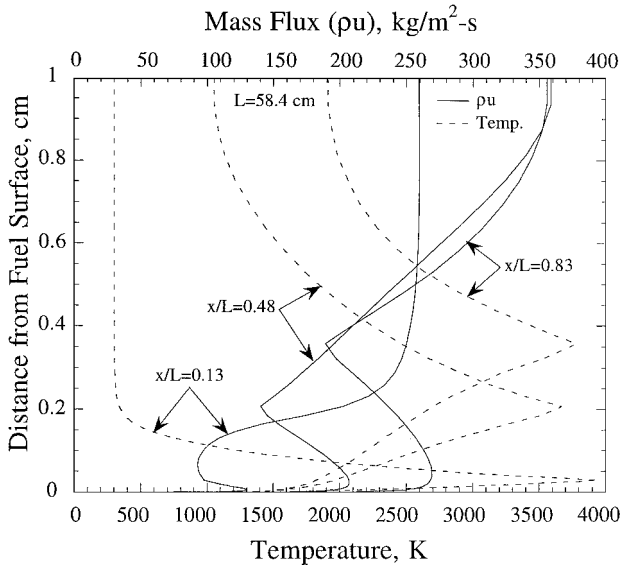

Fig. 13 Calculated gas velocity and temperature profiles.[23]

Because the reaction zone represents the effective boundary for heat transfer to the fuel surface in classical hybrid rocket motors, distortions in the local mass-flux (ρu) profile caused by the presence of the high-temperature reaction zone could affect local Stanton-number behavior. Figure 13 shows a set of calculated gas temperature and mass-flux profiles[24] simulating one of the slab motor test runs of this study. The numerical results at three different axial locations correspond to a time 3.5 s after ignition for the conditions of Test 17. For clarity, the mirror image profiles for the opposing fuel slab are not shown. As expected, the presence of the reaction zone in the boundary layer causes severe temperature gradients. However, the reaction zone also distorts the mass-flux profiles, creating minimum mass fluxes less than that of the core mass fluxes. This effect is stronger near the front of the fuel slab and becomes less pronounced with increasing axial location caused by the increase in average gas temperature from fuel addition and combustion.

Based on the definition of the Stanton number, St is inversely proportional to ρu. The Stanton number can be defined as $St = h/\rho u c_p = Nu_D/Re_D Pr$. As an example, consider that for turbulent pipe flow $Nu_D \sim Re_D^{0.8}$. Combining these two equations shows that $St \sim Re_D^{-0.2}$. Because $Re_D \sim \rho u$, it follows that $St \sim (\rho u)^{-0.2}$. Because the mass flux at the reaction zone in the hybrid boundary layer is lower than that of the boundary-layer edge for the reference case of turbulent pipe flow (at the same Reynolds number), the local Stanton number for the hybrid boundary layer can sometimes exceed the reference Stanton number. It should again be emphasized that both St and St_o were calculated using the local, average G rather than the local value of G at the flame, which is difficult to evaluate analytically. The average value of G, on the other hand, is a conveniently calculated quantity for internal flow situations.

Stanton-number-ratio correlations as a function of both B_{mod} and D_h were obtained for both upstream and downstream flow regimes. The following correlation was found to fit the data for the developed flow region ($x/D_h > 10$, approximately)

$$St/St_0 = \left(0.73 + 9.16B_{\text{mod}}^{-1.6}\right) \cdot (D_h/L)^{0.3} \qquad \text{for} \qquad x/D_h \gtrsim 10 \tag{32}$$

This equation should only be applied to cases in the same range of blowing parameters studied ($2 < B_{\text{mod}} < 7$) as shown in Fig. 12. Figure 14 shows the comparison of the experimental data with the predicted results from Eq. (32); the agreement is within ±10%.

In the developed regime the data with higher values of B_{mod} (above 5, approximately) tend to correlate well with

$$St/St_o = 2B_{\text{mod}}^{-0.73} \tag{33}$$

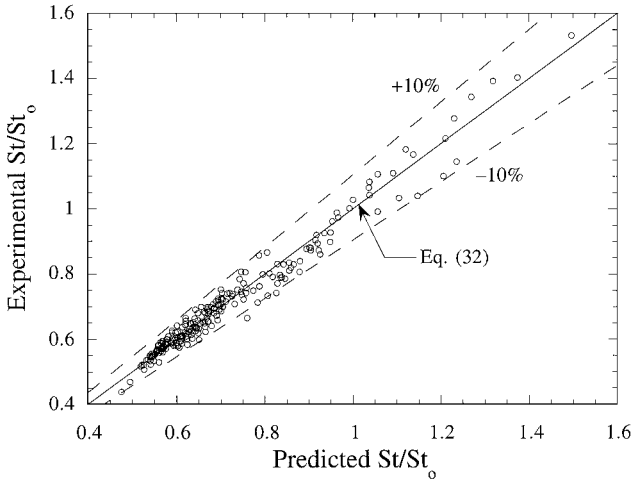

Fig. 14 St/St_o correlation for fully developed flow using Eq. (32).

The power of −0.73 is similar to that of Marxman's −0.77; however, the coefficient of 2 is substantially larger than that of 1.2 shown in Eq. (26), possibly because of the different definitions of G used to calculate St.

Combining Eqs. (25), (28), and (32) to eliminate the Stanton number ratio yields

$$\rho_f r/G = 0.0155(D_h/L)^{0.3}\theta^{0.6}Re_D^{-0.2}\left\{0.73B + 9.16B^{-0.6} \times [\exp(q_r''/q_c'')]^{-1.6}\right\}\left\{1.3(q_r''/q_c'')^{0.75} + \exp\left[-1.3(q_r''/q_c'')^{0.75}\right]\right\} \tag{34}$$

Except for q_r''/q_c'', all other variables in Eq. (34) should be reasonably well known. Though this heat-flux ratio is not usually known a priori, it turns out that the function R of B and q_r''/q_c'', defined by the product of the last two terms on the right side of Eq. (34), where R is given by

$$R[B, (q_r''/q_c'')] = \left\{0.73B + 9.16B^{-0.6}[\exp(q_r''/q_c'')]^{-1.6}\right\} \times \left\{1.3(q_r''/q_c'')^{0.75} + \exp\left[-1.3(q_r''/q_c'')^{0.75}\right]\right\} \tag{35}$$

did not vary much for the tests conducted during this investigation. The values of $R(B, q_r''/q_c'')$ had a mean of 4.73 with a standard deviation of 0.35. The corresponding blowing parameters and ratio of radiant to convective heat fluxes had mean values of 2.1 (standard deviation of 0.18) for B and 0.74 (standard deviation of 0.17) for q_r''/q_c''.

The function defined in Eq. (35) gives a measure of the combined effects of radiation on both fuel regression rate and Stanton-number ratio. The limited range of $R(B, q_r''/q_c'')$ implies that, because the blowing number does not vary greatly, radiant heat transfer tends to act as a self-regulating process by increasing solid-fuel pyrolysis but also reducing convective heat flux as a result of additional wall blowing. This behavior may explain why many previous investigations have not examined radiant heat transfer to any great extent, if at all. An analysis less thorough than that employed here could easily lump the variations of Eq. (35) into an empirically determined constant correlation parameter.

Readers familiar with the hybrid literature may be surprised that the values of B calculated here are somewhat smaller than those cited by previous researchers. For example, Marxman et al. suggested that for acrylic/O_2 systems B is normally between 5 and 10, and thus their regression-rate equations were developed for $B > 5$. Although some differences in the ranges of B cited can be attributed to different propellants, the major factor is probably different definitions of B. The definition employed here includes in the denominator the enthalpy required to heat a unit mass of fuel from its initial value to the pyrolysis temperature. This definition leads to smaller values of B. In addition, Marxman et al. included in the numerator a factor to account for the velocity ratio between the boundary-layer edge

and the flame.[1–3] They assumed that the flame does not affect the velocity profile and that this ratio was therefore about two, which leads to larger values of B. However, as shown by Venkateswaran and Merkle,[24] the streamwise velocity at the flame may exceed the corresponding velocity at the edge of the shear layer. Smoot and Price[7] calculated B values of around 1–2 for rubber/O_2 propellant using a blowing number definition similar to that of the current analysis.

A correlation for the Stanton-number ratio in the developing flow regime was also obtained:

$$St/St_o = \left(0.72 + 8.0B_{\text{mod}}^{-1.3}\right)(D_h/L)^{0.3} \qquad \text{for} \qquad x/D_h \lesssim 10 \tag{36}$$

which is quite similar to the correlation for fully developed flow. Though most of the data fit within a ±10% error band, a good portion was accurate to only ±20%. A developing flow version of Eq. (34) can be obtained by substituting Eq. (36) into Eq. (25). For the developing flow region $R(B, q_r''/q_c'')$, B, and q_r''/q_c'' had mean values of 4.69 (standard deviation of 0.49), 1.8 (standard deviation of 0.15), and 1.3 (standard deviation of 0.46), respectively.

Because both the fully developed and developing Stanton-number correlations had the same mathematical form and similar empirical constants, a third correlation was developed to represent the combined data set from both the upstream and downstream data:

$$St/St_0 = \left(0.65 + 9.56B_{\text{mod}}^{-1.45}\right) \cdot (D_h/L)^{0.3} \tag{37}$$

This overall correlation had about the same accuracy as Eq. (36), but applied over the entire fuel slab. However, using Eq. (37) rather than Eq. (32) for the fully developed data would reduce the accuracy of the Stanton-number prediction for that flow regime from ±10 to ±20%.

Finally, Nusselt-number correlations can be derived by substituting the reference Stanton number [Eq. (24)] into Eqs. (32) and (37) and employing the relationship between the Nusselt and Stanton numbers, $Nu = RePrSt$, yielding

$$Nu_D = \left(0.017 + 0.21B_m^{-1.6}\right) \cdot Re_D^{0.8} Pr^{0.3} (D_h/L)^{0.3} \quad \text{for} \quad x/D_h \gtrsim 10 \tag{38}$$

$$Nu_D = \left(0.016 + 0.18B_{\text{mod}}^{-1.3}\right) \cdot Re_D^{0.8} Pr^{0.3} (D_h/L)^{0.3} \quad \text{for} \quad x/D_h \lesssim 10 \tag{39}$$

Correlation of Literature Data

To test the accuracy of the deduced correlations when applied to other researchers' data, the regression-rate correlation, Eq. (23), with the same values of $a = 0.524$, $b = 0.6$, $c = 1.3$, and $d = 0.75$, was employed to predict experimental data from Shanks and Hudson[18] and Boardman et al.[19] Shanks and Hudson presented a set of results from a series of HTPB/GOX test firings in a tube-geometry, lab-scale hybrid motor. The experimental conditions, in terms of G_o, O/F, p, D, and L, were used in the current data analysis routine to predict the dimensionless regression rate. Because no local regression rates were given, the assumption was made that the average regression rate occurred midway along the fuel grain ($x = 12.7$ cm).

Boardman et al.[19] presented the results of the 11-in. JIRAD motor firings. Although this motor was used to test several fuel port geometries, only the circular port tests were considered during the current study. The JIRAD fuel consisted of about 40% HTPB and 60% Escorez. Therefore, the pyrolysis model given in Ref. 17 for the JIRAD fuel was used in place of the pure HTPB pyrolysis model. However, the soot model developed during the current investigation for pure HTPB was employed because no soot data were available for the JIRAD fuel.

The results of the analysis are shown in Fig. 15 and indicate that Eq. (23) slightly overpredicted the Ref. 18 data by an average of +3.9% (error range of −2.4 to +9%), whereas Ref. 19 data were slightly underpredicted by an average of −5.7% (error range of +0.3 to −10.2%). This error seems reasonable considering the widely different test devices used in the experiments. In comparison, the simple correlation given by Eq. (16) consistently overpredicted the Ref. 19 data by an average of 35%. When applied to the Ref. 18 data, Eq. (16) produced errors between +20 and −10%.

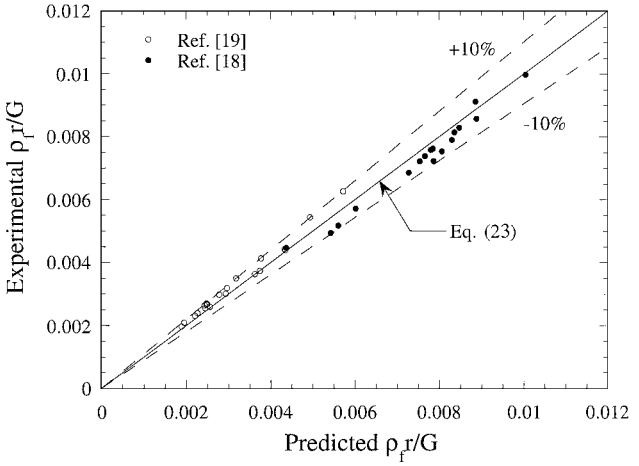

Fig. 15 Correlation for Refs. 18 and 19 data using Eq. (23).

Although both of the motors from Refs. 18 and 19 used circular ports, Shanks and Hudson's motor was of similar scale to the motor used in the present study, but the JIRAD motor grains were approximately five times larger. Thus, Eq. (23), obtained using data from a lab-scale, slab-geometry motor, gave quite reasonable results for a circular-port motor of substantially larger scale. These initial results are encouraging, but more analysis is required to determine the applicability of Eq. (23) to independent data of larger scales. However, these and earlier results of the analysis presented here suggest that mechanistic approaches to regression-rate prediction can be much more accurate than purely empirical correlations, especially when applied to other motors of different scale and geometry. Such methods can account for the various combustion phenomena that govern local solid-fuel regression in hybrid motors, as well as the interactions among these phenomena. For alternate propellant combinations, proper fuel decomposition kinetics, pyrolyzed species concentration profiles, combustion chemistry, and thermal radiation models must be employed to fully analyze the fuel regression-rate behavior.

Conclusions

A semi-empirical approach was developed to assist in correlating the experimental regression rates measured in a lab-scale hybrid rocket motor. The method incorporates experimental hybrid motor results, thermal pyrolysis results, transient, one-dimensional conservation equations, interfacial mass and energy flux balances, algebraic models to calculated radiant heat fluxes, and chemical equilibrium calculations. Regression-rate and heat-transfer correlations were developed to describe the experimental results from the motor firings. The correlations, though complex, offer several insights into regression-rate behavior in hybrid motors because each term has a certain physical significance. The ratio of flame temperature to surface temperature illustrates the effect of variable fluid and transport properties in the boundary layer on regression-rate. The radiant heat flux also plays an important role in the overall regression process: radiation from soot and gas-phase combustion products increases the regression rate, but this increase in gas blowing also blocks convective heat transfer, as shown explicitly by the Stanton-number correlations. In addition, the Stanton-number-ratio correlations indicate that the internal, accelerating flow with combustion and variable fluid properties sometimes have larger convective heat-transfer rates than the reference flows, even in the presence of wall blowing. Depending upon the flow regime (developing or fully developed), different correlations of Stanton number with blowing parameter and dimensionless length scale were necessary to accurately represent the data. The correlations adequately predicted regression rates from circular-port geometry hybrid motors

of both laboratory and large scales used by other researchers. Simple expressions such as $r = aG^n$ do not adequately represent the boundary-layer combustion processes and produced significantly larger errors than the correlations developed here when applied to independent experimental data. The results of this investigation suggest that fuel regression behavior can be accurately predicted when proper combustion chemistry, radiation, and fuel pyrolysis models are combined with scientific correlations that account for the complex boundary-layer processes governing local solid-fuel regression rates in hybrid rocket motors.

Acknowledgments

The authors would like to thank both NASA Headquarters and the NASA Propulsion Engineering Research Center at the Pennsylvania State University for supporting Martin Chiaverini's doctoral research activities with a NASA Traineeship. His support from the Pennsylvania Space Grant Consortium is also very highly appreciated.

References

[1]Marxman, G. A., and Gilbert, M., "Turbulent Boundary Layer Combustion in the Hybrid Rocket," *Ninth International Symposium on Combustion*, Academic, New York, 1963, pp. 371–383.

[2]Marxman, G. A., Wooldridge, C. E., and Muzzy, R. J., "Fundamentals of Hybrid Boundary Layer Combustion," *Heterogeneous Combustion*, edited by H. G. Wolfhard, I. Glassman, and L. Green, Jr., Vol. 15, Progress in Astronautics and Aeronautics, Academic, New York, 1964, pp. 485–521.

[3]Marxman, G. A., "Combustion in the Turbulent Boundary Layer on a Vaporizing Surface," *Tenth (International) Symposium on Combustion*, Combustion Inst., Pittsburgh, PA, 1965, pp. 1337–1349.

[4]Paul, P. J., Mukunda, H. S., and Jain, V. K., "Regression Rates in Boundary Layer Combustion," *Nineteenth (International) Symposium on Combustion*, Combustion Inst., Pittsburgh, PA, 1982, pp. 717–729.

[5]Estey, P. N., Altman, D., and McFarlane, J. S., "An Evaluation of Scaling Effects for Hybrid Rocket Motors," AIAA Paper 91-2517, June 1991.

[6]Strand, L. D., Jones, M. D., Ray, R. L., and Cohen, N. S., "Characterization of Hybrid Rocket Internal Heat Flux and HTPB Fuel Pyrolysis," AIAA Paper 94-2876, June 1994.

[7]Smoot, L. D., and Price, C. F., "Regression Rates of Nonmetalized Hybrid Fuel Systems," *AIAA Journal*, Vol. 3, No. 8, 1965, pp. 1408–1413.

[8]Smoot, L. D., and Price, C. F., "Regression Rates of Metalized Hybrid Fuel Systems," *AIAA Journal*, Vol. 4, No. 5, 1965, pp. 910–915.

[9]Smoot, L. D., and Price, C. F., "Pressure Dependence of Hybrid Fuel Regression Rates," *AIAA Journal*, Vol. 5, No. 1, 1966, pp. 102–106.

[10]Kosdon, F. J., and Williams, F. A., "Pressure Dependence of Nonmetalized Hybrid Fuel Regression Rate," *AIAA Journal*, Vol. 5, No. 4, 1967, pp. 774–777.

[11]Muzzy, R. J., "Applied Hybrid Combustion Theory," AIAA Paper 72-1143, Nov. 1972.

[12]Rastogi, R. P., and Deepak, D., "Pressure Dependence of Hybrid Fuel Burning Rate," *AIAA Journal*, Vol. 14, No. 7, 1976, pp. 988–990.

[13]Kumar, R. N., and Stickler, D. B., "Polymer-Degradation Theory of Pressure-Sensitive Hybrid Combustion," *Thirteenth (International) Symposium on Combustion*, Combustion Inst., Pittsburgh, PA, 1971, pp. 1059–1072.

[14]Miller, E., "Hybrid Rocket Combustion Regression Rate Model," *AIAA Journal*, Vol. 4, No. 4, 1966, pp. 752, 753.

[15]Chiaverini, M. J., Serin, N., Johnson, D. K., Lu, Y. C., and Kuo, K. K., "Instantaneous Regression Behavior of HTPB Solid Fuels Burning with GOX in a Simulated Hybrid Rocket Motor," *Challenges in Propellants and Combustion 100 Years After Nobel*, edited by K. K. Kuo et al., Begell House, New York, 1997, pp. 719–733.

[16]Chiaverini, M. J., Johnson, D. K., Serin, N., Lu, Y. C., Kuo, K. K., and Risha, G. A., "Regression Rate Behavior of Hybrid Rocket Solid Fuels," *Journal of Propulsion and Power*, Vol. 16, No. 1, 2000, pp. 125–132.

[17]Chiaverini, M. J., Harting, G. C., Lu, Y. C., Kuo, K. K., Peretz, A., Jones, S., Wygle, B., and Arves, J. P., "Pyrolysis Behavior of Hybrid Rocket Solid Fuels Under Rapid Heating Conditions," *Journal of Propulsion and Power*, Vol. 15, No. 6, 1999, pp. 888–895.

[18]Shanks, R. B., and Hudson, M. K., "The Design and Control of a Lab-scale Hybrid Rocket Facility for Spectroscopy Studies," AIAA Paper 94-3016, June 1994.

[19]Boardman, T. A., Carpenter, R. L., Goldberg, B. E., and Shaeffer, C. W., "Development and Testing of 11- and 24-Inch Hybrid Motors Under the Joint Government/Industry IR&D Program," AIAA 93-2552, June 1993.

[20]Reid, R. C., Prausnitz, J. M., and Poling, B. E., *The Properties of Gases and Liquids*, McGraw–Hill, New York, 1987, p. 657.

[21]Cohen, N. S., Fleming, R. W., and Derr, R. L., "Role of Binders in Solid Propellant Combustion," *AIAA Journal*, Vol. 12, No. 2, 1974, pp. 212–218.

[22]Incropera, Frank P., and DeWitt, David P., *Fundamentals of Heat and Mass Transfer*, 3rd ed., Wiley, New York, 1990, pp. 827, 828.

[23]Modest, M. F., *Radiative Heat Transfer*, McGraw–Hill, New York, 1993, pp. 349–369.

[24]Venkateswaran, S., and Merkle, C. L., "Size Scale-Up in Hybrid Rocket Motors," AIAA Paper 96-0647, Jan. 1996.

[25]Gibson, C. H., and Libby, P. A., *Combustion Science and Technology*, Vol. 6, 1972, p. 29.

[26]Kuo, K. K., *Principles of Combustion*, Wiley, New York, 1986, pp. 668–672.

[27]Cheng, G. C., Farmer, R. C., Jones, H. S., and McFarlane, J. S., "Numerical Simulation of the Internal Ballistics of a Hybrid Rocket Motor," AIAA 94-0554, Jan. 1994.

[28]Turns, S. R., *An Introduction to Combustion: Concepts and Applications*, McGraw–Hill, New York, 1996, pp. 362–367.

[29]Strand, L., Ray, R., Anderson, F., and Cohen, N., "Hybrid Rocket Fuel Combustion and Regression Rate Study," AIAA Paper 92-3302, July 1992.

[30]Chiaverini, Martin J., "Regression Rate and Pyrolysis Behavior of HTPB-Based Solid Fuels in a Hybrid Rocket Motor," Ph.D. Dissertation, Dept. of Mechanical Engineering, Pennsylvania State Univ., Univ. Park, PA, Dec. 1997.

[31]Lengellé, G., Simon, P., Heslouin, A., and Seillier, S., "Operating of Hybrid Propulsion for Space Applications," *3rd International Symposium on Space Propulsion*, Beijing, Aug. 1997.

[32]Lees, L., *Combustion and Propulsion, Third AGARD Colloquium*, Pergamon, 1958, p. 451.

[33]Green, L., "Introductory Considerations on Hybrid Rocket Combustion," *Heterogeneous Combustion*, edited by H. G. Wolfhard, I. Glassman, and L. Green, Jr., Vol. 15, Progress in Astronautics and Aeronautics, Academic, New York, 1964, pp. 451–484.

[34]Kays, W. M., and Crawford, M. E., *Convective Heat and Mass Transfer*, 2nd ed., McGraw–Hill, New York, 1980, p. 277.